Research Article

Nano Research
2021, 14(4): 1218–1227

ISSN 1998-0124 CN 11-5974/O4
https://doi.org/10.1007/s12274-020-3221-y

Fabrication of Fe nanocomplex pillared few-layered $Ti_3C_2T_x$ MXene with enhanced rate performance for lithium-ion batteries

Pengfei Huang, Shunlong Zhang, Hangjun Ying, Wentao Yang, Jianli Wang, Rongnan Guo, and Weiqiang Han (✉)

School of Materials Science and Engineering, Zhejiang University, Hangzhou 310027, China

Received: 2 September 2020 / **Revised:** 18 October 2020 / **Accepted:** 1 November 2020

ABSTRACT

Pillaring technologies have been considered as an effective way to improve lithium storage performance of $Ti_3C_2T_x$ MXene. Nevertheless, the pillared hybrids suffer from sluggish Li^+ diffusion kinetics and electronic transportation due to the compact multi-layered MXene structure, thus exhibiting inferior rate performance. Herein, the few-layered Ti_3C_2 MXene (f-Ti_3C_2 MXene) which is free from restacking can be prepared quickly based on the NH_4^+ ions method. Besides, Fe nanocomplex pillared few-layered $Ti_3C_2T_x$ (FPTC) heterostructures are fabricated via the intercalation of Fe ions into the interlayer of f-Ti_3C_2 MXene. The f-Ti_3C_2 MXene which is immune to restacking can provide a highly conductive substrate for the rapid transport of Li^+ ions and electrons and possess adequate electrolyte accessible area. Moreover, f-Ti_3C_2 MXene can efficiently relieve the aggregation, prevent the pulverization and buffer the large volume change of Fe nanocomplex during lithiation/delithiation process, leading to enhanced charge transfer kinetics and excellent structural stability of FPTC composites. Consequently, the FPTC hybrids exhibit a high capacity of 535 mAh·g^{-1} after 150 cycles at 0.5 A·g^{-1} and an enhanced rate performance with 310 mAh·g^{-1} after 850 cycles at 5 A·g^{-1}. This strategy is facile, universal and can be extended to fabricate various few-layered MXene-derived hybrids with superior rate capability.

KEYWORDS

Fe ions intercalation, few-layered MXene, pillared MXene, lithium-ion batteries

1 Introduction

In recent years, the discovery of two-dimensional (2D) layered materials, including graphene [1] and dichalcogenides [2], have greatly enhanced the performance of energy storage systems (ESSs) because of their exceptional electrical conductivity, favorable chemical stability and preferable specific surface area [3]. Transition metal nitrides and carbides termed MXenes, a new member of 2D layered materials, were first synthesized by Gogotsi' group in 2011 [4], which possess a formula of $M_{n+1}X_nT_x$ (Where M = Ti, Nb, Sc, V, Ta, etc; X=C, N; T = –O, –OH, –F; n = 1–3). They were typically fabricated by selective etching of the A layers from their parent MAX phase (A = Al, Si, Ga, Ge, etc.) [5]. MXenes have aroused broad interests as potential electrode materials for lithium-ion batteries (LIBs) [6] and other metal-ion batteries (e.g., Na^+ [7, 8], K^+ [9], Zn^{2+} [10], and Al^{3+} [11]) on account of their layered structure, high metallic conductivity and unique surface chemistry.

As the most extensively studied MXene, Ti_3C_2 delivers a moderate theoretical capacity of 320 mAh·g^{-1} based on density functional theory [12], which is considerably lower than that of Si (4,200 mAh·g^{-1}) [13], Sn (994 mAh·g^{-1}) [14], and Ge (1,624 mAh·g^{-1}) [15] etc. Moreover, surface terminated groups (such as –F, –O and –OH) greatly limit its electrochemical performance, thus leading to a quite low specific capacity [12, 16, 17]. Continued efforts have been devoted to tackling this obstacle up to now. One feasible solution to substantially improve the practical capacity of MXene is to prepare MXene-based composites with electrochemically active materials [8, 18–24], especially pillared MXene with other active materials [25–27]. For instance, V_2C@Co electrode demonstrated a superior capacity of 1,117.3 mAh·g^{-1} at 0.1 A·g^{-1} owing to the augmented interlayer distance and strong V–O–Co bonding [25]. Sn(IV)@Ti_3C_2 anode with ultralarge interlayer spacing showed a capacity of 506 mAh·g^{-1} after 250 cycles at 1 A·g^{-1} [27]. Above-mentioned examples have confirmed that pillared structures have markedly advanced the progress of MXenes [28]. However, the reported pillared MXene-based composites are trapped in multi-layered state, thus resulting in mediocre rate performance. It is believed that more pillared heterostructures are highly required to further enhance the lithium storage performance of MXenes, especially for pillared few-layered MXenes.

High-rate capability is a crucial indicator for future promising batteries due to the rapid advance of ESSs and electric vehicles market [29]. Nevertheless, batteries possessing outstanding rate performance are perplexed by compromised specific capacity. Therefore, fabrication of composite electrodes combining excellent rate capability and high specific capacity is a top priority. It is well-known that rate capability of electrode is closely related to Li^+ ions diffusion kinetics. According to the following equation [30]

$$t = L^2/2D \quad (1)$$

where t means diffusion time, D denotes the diffusion coefficient and L stands for diffusion length. It can be concluded that reducing the size dimensions of the electrode can be an

Address correspondence to hanwq@zju.edu.cn

efficient method to considerably enhance the rate performance [31]. The most pivotal point for superior rate capability lies in the fast transport of electrons and Li^+ ions to the surface of 2D materials, instead of sluggish Li^+ diffusion in the solid phase [32]. However, MXene-based heterostructures are obsessed by inferior rate capability because of compact multi-layered structure [25, 27], which do not possess enough surface active sites and electrolyte accessible area, thus manifesting mediocre rate performance [33, 34]. Besides, the most frustrating thing is that the few-layered MXenes suffer from serious restacking phenomenon during preparation process [35], which greatly hinders their development and potential for fabricating heterostructures with other high theoretical capacity materials. Therefore, it is of great significance that pillared few-layered MXene heterostructures can be prepared facilely.

Herein, we synthesized the f-Ti_3C_2 MXene rapidly and facilely which is immune to restacking phenomenon via the introduction of NH_4^+ ions and then fabricated Fe nanocomplex pillared few-layered $Ti_3C_2T_x$ (denoted as FPTC) composites through cetyltrimethylammonium bromide (CTAB) pre-pillaring and Fe^{3+} ions pillaring method. Fe^{3+} ions can easily insert into interlayer of f-Ti_3C_2 MXene based on the pre-intercalation of CTAB which expands the interlayer spacing. The f-Ti_3C_2 MXene can act as conductive and elastic matrixes to facilitate the electronic transfer and ionic diffusion and cushion the large volume change of Fe nanocomplex during lithiation/delithiation process. Benefiting from not only the synergistic effect between f-Ti_3C_2 MXene and the high theoretical capacity of Fe nanocomplex (Fe_2O_3), but also the presence of *in-situ* formed TiO_2 by partial oxidation of f-Ti_3C_2 MXene which can stabilize the electrode structure owing to its mechanical and electrochemical stability, the as-prepared FPTC electrode delivers a high reversible capacity of 535 mAh·g^{-1} after 150 cycles at 0.5 A·g^{-1} and an outstanding rate performance with 310 mAh·g^{-1} after 850 cycles at 5 A·g^{-1}.

2 Experimental section

2.1 Materials

Ti_3AlC_2 powders (> 98% purity, 500 mesh) were supplied by Forsman Co., Ltd. Hydrofluoric acid (HF, 50%) solutions, tetramethylammonium hydroxide (TMAOH, 25%), $FeCl_3·6H_2O$ powder and ammonium hydroxide (25%) were purchased from Aladdin Reagent. CTAB was provided by Macklin.

2.2 Synthesis of multi-layered Ti_3C_2 MXene

Multi-layered Ti_3C_2 was synthesized by selective etching of Al layers from Ti_3AlC_2 powder. Firstly, 4 g of the Ti_3AlC_2 powder was immersed in 40 mL of HF solutions at ambient temperature for 24 h. Then the solution was repetitively centrifuged at 8,000 rpm for 5 min and washed with deionized water until the pH of supernatant reached 6–7. Finally, the multi-layered Ti_3C_2 powder was obtained by freeze-drying for 12 h.

2.3 Synthesis of f-Ti_3C_2 MXene

$Ti_3C_2T_x$ powder (0.5 g) was introduced in 8 mL of TMAOH and the mixture was stirred under room temperature for 10 h to disperse $Ti_3C_2T_x$ flakes. The intermediate product was then obtained by high-speed centrifugation at 5,000 rpm for 5 min and 50 mL of deionized water was added to the above product. The solution was ultrasonicated for 2 h and centrifuged at 4,000 rpm for 5 min and the supernatant was collected. It is necessary that a small quantity of f-Ti_3C_2 MXene which have been ultrasonicated completely should be segregated timely from the solution by subsequent centrifugation. Then 10 mL of ammonium hydroxide was introduced in the supernatant and f-Ti_3C_2 MXene would precipitate owing to electrostatic precipitation. Deionized water was removed and the sediment was freeze-dried. Finally, the f-Ti_3C_2 MXene was obtained by annealing at 200 °C for 2 h to entirely remove the ammonium hydroxide.

2.4 Synthesis of FPTC composites

F-Ti_3C_2 MXene powder was first immersed in 50 mL of CTAB solution (0.4 wt.%) at 40 °C for 24 h. Then 0.15 g of $FeCl_3·6H_2O$ was transferred to the above solution at 40 °C for another 48 h and the mixture was collected by freeze-drying. Finally, FPTC hybrids was obtained by annealing at 300 °C for 2 h in argon atmosphere.

2.5 Materials characterization

The morphology and structure were carried out by field-emission scanning electron microscope (FESEM, SU-80, Hitachi Ltd., Japan). The transmission electron microscope (TEM) images, high-resolution transmission electron microscope (HRTEM) images, selected area electron diffraction (SAED) pattern and scanning transmission electron microscopy (STEM) elemental mapping images were obtained by a TEM (200 kV, Tecnai G^2 F20 S-TWIN, FEI Ltd). The phase structures were characterized by X-ray diffraction (XRD, Bruker, Cu Kα radiation = 0.154 nm, a step scan of 0.02°). The surface bonding properties were obtained by an X-ray photoelectron spectrometer (XPS) (Axis Ultra DLD, USA). The specific surface area and pore structure were analyzed by Micromeritics ASAP 2020 Plus HD88. Zeta potential was characterized by a Zeta sizer (Nano-ZS) at room temperature. The element contents were quantified by Inductively coupled plasma-Mass Spectrometry (ICP-MS) (PerkinElmer NexION 300X, iCAP6300).

2.6 Electrochemical measurements

The electrochemical performance was investigated by using CR2032-type coin cells which were assembled with metallic lithium sheet as both the reference and counter electrodes in an argon-filled glovebox. The electrodes were prepared by mixing FPTC powder with carbon black (Super P) and carboxymethylcellulose sodium (CMC) binder in deionized water with a weight ratio of 8:1:1. The slurry was casted onto the copper foil and then dried in a vacuum oven under 70 °C for 12 h. The specific capacity is calculated based on all the components in the active materials, i.e., the mass of Fe_2O_3 + TiO_2 + f-Ti_3C_2 hybrids. The electrochemical tests were conducted with $LiPF_6$ in dimethyl carbonate (EC)/ethylmethyl carbonate (EMC) /fluoroethylene carbonate (FEC) electrolyte in a 1:1:1 volume ratio. The discharge-charge test was conducted on a Land (CT2001A) battery test system between 0.01 and 3.0 V at 30 °C. Cyclic voltammetry (CV) at each scan rates between 0.01 and 3 V and electrochemical impedance spectroscopy (EIS) with the frequency range from 0.01 to 10^6 Hz were operated on an electrochemical workstation (Solartron Analytical, UK).

3 Results and discussion

A schematic illustration for fabricating FPTC heterostructures is exhibited in Fig. 1. Firstly, the Ti_3AlC_2 MAX phases were etched by 50% HF solution at ambient temperature for 24 h to obtain multi-layered Ti_3C_2 MXene. Then, the f-Ti_3C_2 MXene was prepared via continuous ultrasonication and then precipitated through the introduction of NH_4^+ based on electrostatic precipitation. As followed, the f-Ti_3C_2 MXene powders were

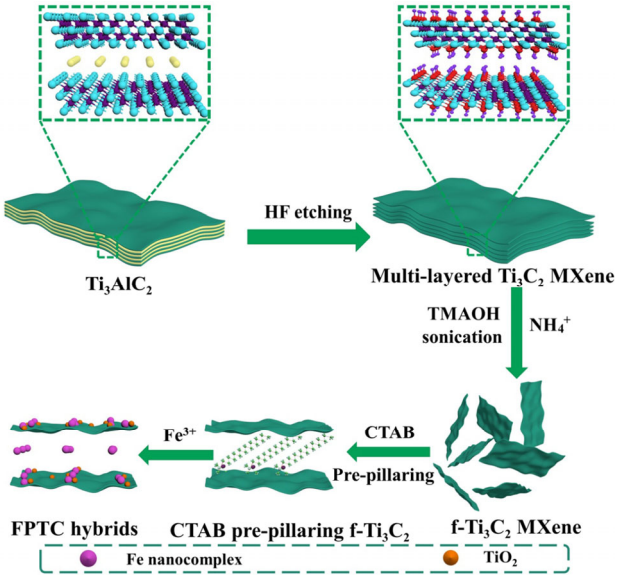

Figure 1 Schematic illustration of the synthesis of FPTC composites.

immersed into CTAB solution, which can increase interlayer spacing of f-Ti_3C_2 by CTAB pillaring process. Fe ions can then insert into the interlayer of f-Ti_3C_2 MXene or be absorbed at the surface of MXene matrix via the introduction of $FeCl_3{\cdot}6H_2O$. The related change can also be reflected in the result of zeta potential (Table S1 in the Electronic Supplementary Material (ESM)). Finally, the FPTC composite was obtained by annealing at 300 °C for 2 h in argon atmosphere.

The XRD patterns of Ti_3AlC_2 powder, f-Ti_3C_2 MXene and FPTC hybrids are illustrated in Figs. 2(a) and 2(b). For the Ti_3AlC_2 powder (Fig. 2(a)), the main diffraction peaks situated at 9.6° and 39.1° corresponded to the (002) and (104) plane [18], respectively, which is fitted well with those of Ti_3AlC_2 (JCPDS 52-0875). There is a significant loss in crystallinity after HF etching. The peak located at 2θ = 39.1° disappeared suggesting the effective etching of Al layers [4], and the peak at 2θ = 9.6° shifted from 9.6° to 9.06° indicating an expansion of interlayer spacing from 9.19 to 9.75 Å (Fig. 2(b)) [36]. After the CTAB pre-pillaring process, Fe ions were intercalated into f-Ti_3C_2 MXene matrix. The characteristic peak at 2θ = 9.6° shifted to 8.86° and partly to 5.72°, corresponding to the interplanar spacing of 9.96 Å and 15.43 Å, respectively. The huge shift of (002) peak to 5.72° is reasonable when compared with previously reported works [27, 37–40], which further confirmed the pillared structure of FPTC hybrids was successfully prepared (Fig. 2(b)). As for the prepared FPTC heterostructures (Fig. 2(a)), some peaks located around 2θ = 27.51°, 32.77°, and 41.26° belongs to Fe_2O_3 compound (JCPDS 16-0653). The peaks located at 25.3°, 36.06°, 38°, 48°, 54.18°, 56.5° and 68° can be indexed to *in-situ* formed TiO_2 due to partial oxidation of f-Ti_3C_2 MXene during the preparation process [35, 41]. In fact, the f-Ti_3C_2 MXene can be oxidized to form TiO_2 [42, 43].

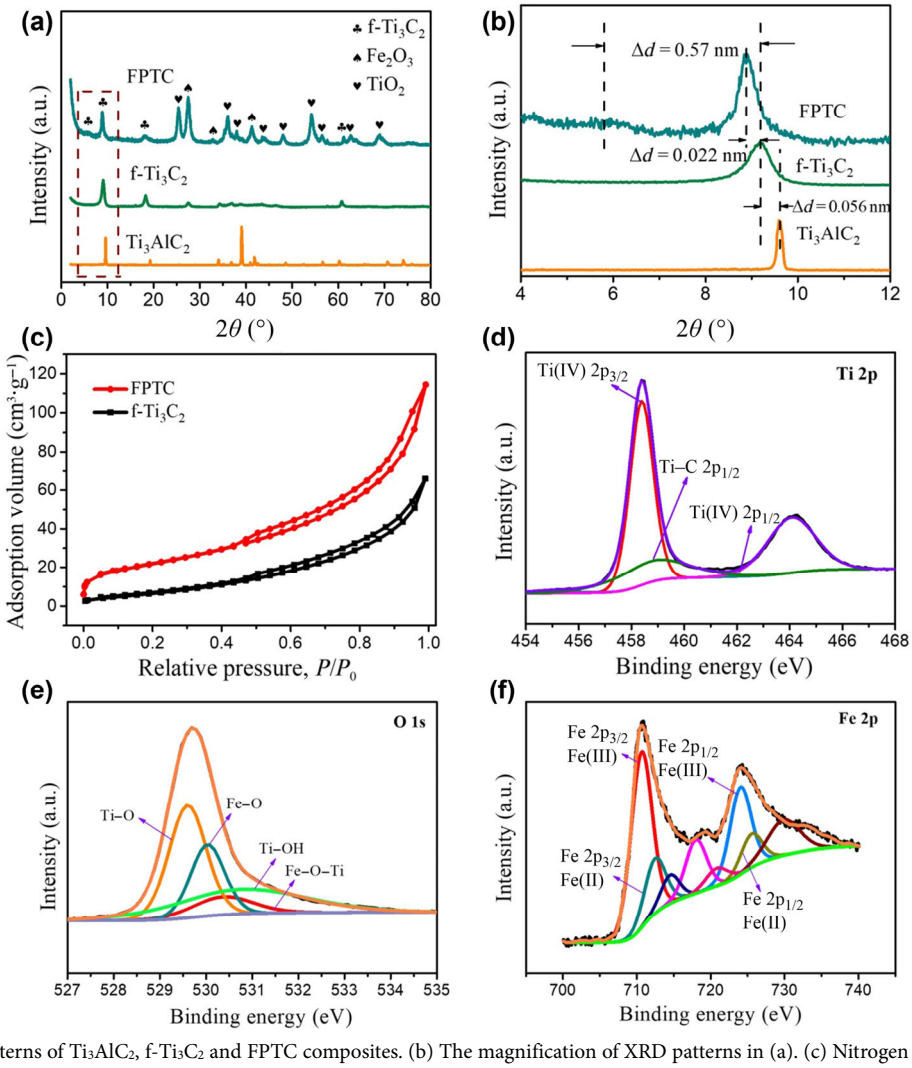

Figure 2 (a) XRD patterns of Ti_3AlC_2, f-Ti_3C_2 and FPTC composites. (b) The magnification of XRD patterns in (a). (c) Nitrogen sorption isotherm plots of f-Ti_3C_2 and FPTC composites. (d) Ti 2p spectrum, (e) O 1s spectrum and (f) Fe 2p spectrum of FPTC samples.

Generally, the oxidation of f-Ti_3C_2 MXene starts from the edges and TiO_2 grows throughout the entire surface. Additionally, single MXene flakes with small lateral size are more easily oxidized compared with multi-layered flakes [42]. Fortunately, the *in-situ* generation of TiO_2 can prevent the agglomeration and pulverization of Fe nanocomplex during electrochemical processes owing to excellent mechanical and electrochemical stability of TiO_2 [44, 45].

The surface area and pore structure of FPTC hybrids and f-Ti_3C_2 MXene are characterized by nitrogen adsorption analysis. There is obvious hysteresis loop for both of them (Fig. 2(c)). F-Ti_3C_2 MXene possesses a specific surface area of 25.6 $m^2 \cdot g^{-1}$, which far exceeds that of pristine Ti_3AlC_2 powder (2.0 $m^2 \cdot g^{-1}$) [46]. For the FPTC hybrids, it exhibits a specific surface area of 79.6 $m^2 \cdot g^{-1}$ higher than that of f-Ti_3C_2 MXene, which can be assigned to the pillaring of Fe nanocomplex, thus exploiting more active sites for adsorption and desorption. As shown in Fig. S1(a) in the ESM, both of f-Ti_3C_2 and FPTC hybrids deliver a pore size distribution within the limits of 2–35 nm and center at about 4 nm according to Barrett–Joyner–Halenda method. The higher specific surface area and porosity of FPTC composites can greatly enhance the ionic and electronic accessibility owing to the abundant active sites and enlarged interface area between electrolyte and electrode, which can significantly enhance its rate performance [47–49].

The valence states of Ti, C, Fe, O elements of f-Ti_3C_2 MXene and FPTC composites conducted by XPS analysis are schematically illustrated in Figs. 2(d)–2(f) and Figs. S1(b)–S1(d) in the ESM. For f-Ti_3C_2 MXene, the signal of Ti 2p, O 1s, C 1s, F 1s can be examined except for Al 2p (Fig. S1(b) in the ESM), reconfirming the successful etching of Al layers from Ti_3AlC_2 powder. Meanwhile, the Fe 2p signal can be detected for FPTC heterostructures. As shown in Figs. 2(d)–2(f), the Fe 2p and Ti 2p spectrum can be fitted into $2p_{1/2}$ and $2p_{3/2}$ doublets because of the effect of spin-orbit coupling [25]. Ti 2p spectrum shows four main peaks located at 455.1, 458.0, 458.8 and 464.0 eV, (Fig. 2(d)) which can be assigned to Ti-C $2p_{3/2}$, Ti(IV) $2p_{3/2}$, Ti-C $2p_{1/2}$, Ti(IV) $2p_{1/2}$, respectively [50, 51]. For f-Ti_3C_2 MXene, it can also be fitted into six main peaks situated at 455.1, 455.7, 456.8, 458.8, 461.2, 462.3 eV, corresponding to Ti-C $2p_{3/2}$, Ti(II) $2p_{3/2}$, Ti(III) $2p_{3/2}$, Ti-C $2p_{1/2}$, Ti(II) $2p_{1/2}$ and Ti(III) $2p_{1/2}$ (Fig. S1(c) in the ESM), respectively [50]. The Ti 2p spectrum of FPTC hybrids is different from that of pure f-Ti_3C_2 due to the partial oxidation of MXene. The O 1s spectrum of FPTC hybrids exhibited in Fig. 2(e) reveals four peaks centered at 529.6, 529.9, 530.3 and 530.8 eV, ascribed to Ti-O, Fe-O, Ti-O-Fe and Ti-OH, respectively [18, 52–54]. The formation of Fe-O-Ti covalent bonding can stabilize the electrode structure and contribute to the superior cycling performance of FPTC composites [13, 25]. As for f-Ti_3C_2 MXene, the O 1s spectrum can be fitted into three main peaks situated at 529.4, 530.3 and 531 eV, corresponding to Ti-O, -OH and Ti-OH (Fig. S1(d) in the ESM), respectively [52, 54]. As shown in Fig. 2(f), the Fe 2p spectrum of FPTC hybrids can be divided into four main peaks situated at 710.8, 711.9, 724.7 and 725.2 eV, which can be assigned to Fe(III) $2p_{3/2}$, Fe(II) $2p_{3/2}$, Fe(III) $2p_{1/2}$ and Fe(II) $2p_{1/2}$, respectively [18, 55]. The positive shift of binding energy of Fe (III) $2p_{3/2}$ from 710.7 eV (Fe (III) $2p_{3/2}$ of Fe_2O_3) to 710.8 eV further confirms the formation of Fe-O-Ti bond in FPTC hybrids [53, 56]. The other peaks located at 715, 718.2, 720 and 730.5 eV can be attributed to satellite peaks [57–60]. The deconvolution result exhibits two valence states corresponding to Fe^{2+} and Fe^{3+}, and the emergence of Fe^{2+} might be ascribed to the reduction of Fe^{3+} by low valence Ti [61]. It can be calculated that the proportion of Fe^{3+} (23.3 %) to Fe^{2+} (11.7 %) is 1.95:1 based on XPS analysis, which reveals that the content of Fe^{3+} are much higher than that of Fe^{2+}. Besides, the amount of Fe ions in FPTC hybrids is 11.61 wt.% confirmed by ICP-MS.

The morphology of Ti_3AlC_2 MAX and multi-layered Ti_3C_2 MXene is illustrated in Fig. S2 in the ESM. It can be seen that Ti_3AlC_2 MAX possesses the classical densely layered structure. Layers are separated from each other after HF etching and typical accordion-like structure is observed for multi-layered Ti_3C_2 MXene [62]. The SEM images of f-Ti_3C_2 MXene are exhibited in Figs. 3(a) and 3(b) and Figs. S3(a) and S3(b) in the ESM. A panoramic image indicates the number of layers of MXene decreases dramatically from thousand layers to several layers with a lateral size of 2–3 μm. More importantly, f-Ti_3C_2 MXene can be distributed uniformly without aggregation phenomenon (Fig. 3(a)), which is beneficial to the intercalation of CTAB and Fe ions. As shown in Fig. S3(c) in the ESM, it can be observed that f-Ti_3C_2 MXene can precipitate via the addition of NH_4^+ ions based on electrostatic interaction between

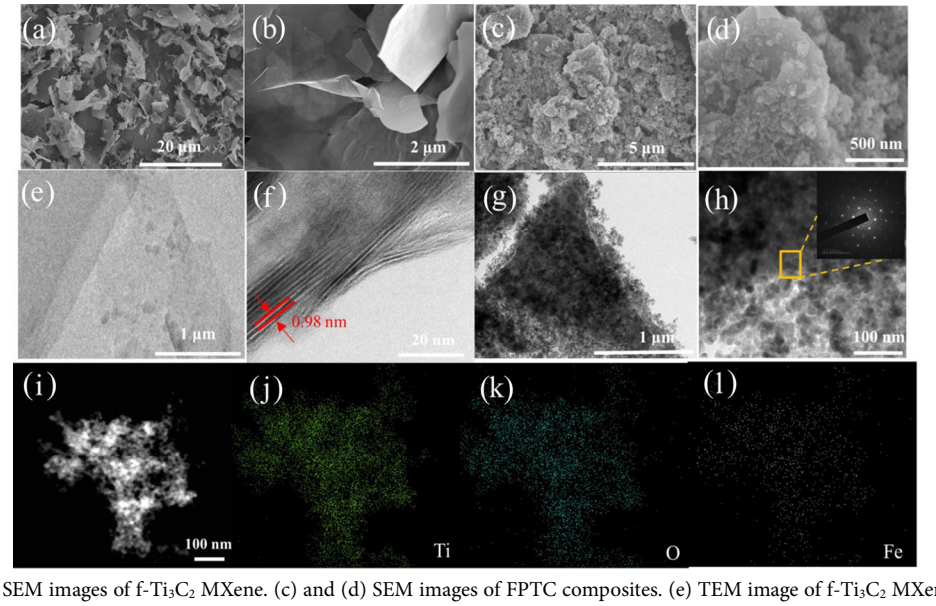

Figure 3 (a) and (b) SEM images of f-Ti_3C_2 MXene. (c) and (d) SEM images of FPTC composites. (e) TEM image of f-Ti_3C_2 MXene. (f) HRTEM image of f-Ti_3C_2 MXene. (g) and (h) TEM images of FPTC composites, the inset corresponds to SAED image of FPTC composites. (i)–(l) STEM image of FPTC composites and corresponding elemental mapping.

the positive-charged NH_4^+ ions and negative-charged f-Ti_3C_2 MXene, significantly shortening the time to fully freeze-dry the f-Ti_3C_2 MXene, which is similar to other group's recent findings that Fe^{2+} ions can also lead to fast gelation of Ti_3C_2 [63]. However, the greatest advantage of our method is that ammonium hydroxide can be removed by annealing. Thus, NH_4^+ cannot affect the electrochemical performance of electrode. More importantly, the yield of f-Ti_3C_2 MXene is around 56%, which is greatly higher than traditional preparation method. Above discussion confirms that a certain amount of high-quality f-Ti_3C_2 MXene can be obtained quickly by this facile method (Fig. S3(d) in the ESM). The SEM images of FPTC hybrids in Figs. 3(c) and 3(d) reveal the Fe nanocomplexes (Fe_2O_3) are anchored on the surface of f-Ti_3C_2 MXenes or intercalated into the interlayers. The microstructures of f-Ti_3C_2 MXene and FPTC hybrids are further analyzed by TEM and HRTEM, as demonstrated in Fig. 3(e), an ultrathin Ti_3C_2 nanosheet with a lateral size of 2–3 μm can be observed, which is consistent with SEM results (Fig. 3(b)). The HRTEM image of f-Ti_3C_2 MXene shown in Fig. 3(f) clearly exhibits the layered structure. The overall thickness of f-Ti_3C_2 MXene has been dramatically decreased to 1–10 nm and the interlayer distance is about 0.98 nm, which reconfirms that the preparation method of f-Ti_3C_2 MXene in this work is indeed feasible. As shown in Figs. 3(g) and 3(h), the uniform distribution of Fe nanocomplexes on the surface or in the interlayer of f-Ti_3C_2 MXene can be observed. More importantly, the size of Fe nanocomplex is about 10–20 nm. Thus, it is believed that the Li^+ ions diffusion kinetics and electronic transfer can be considerably accelerated due to the shortened ionic diffusion and electronic transport pathway [30]. The SAED pattern of FPTC hybrids shown in Fig. S4 in the ESM manifests that both of f-Ti_3C_2 MXene and Fe nanocomplexes possess good crystallinity. The element distribution is illustrated in Figs. 3(i)–3(l), it reveals that titanium, oxygen and iron elements are homogeneously distributed within the FPTC composites.

The CV curve of FPTC heterostructures at 0.1 mV·s^{-1} within a voltage range from 0.01 to 3 V is shown in Fig. 4(a). It can be seen that three peaks positioned at about 1.35, 1.04 and 0.71 V are discovered in the first cathodic process. The peak at 1.35 V is

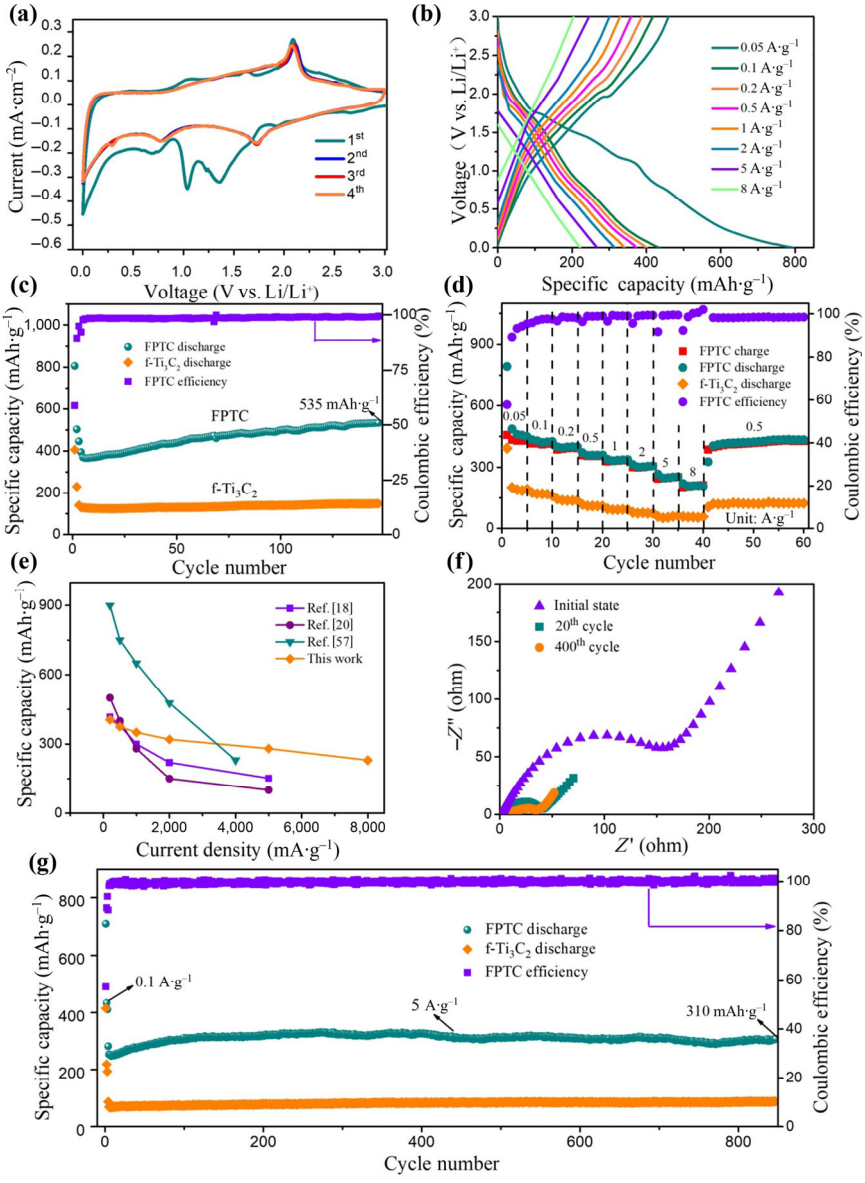

Figure 4 (a) CV curve of FPTC electrodes from 3.0 to 0.01 V vs. Li/Li$^+$ at a scan rate of 0.1 mV·s^{-1}. (b) Discharge-charge curves of FPTC electrodes at different current densities. (c) Cycling performance of f-Ti_3C_2 and FPTC composites at 0.5 A·g^{-1}. (d) Rate performance of f-Ti_3C_2 and FPTC electrodes. (e) Rate performance comparison of different MXene-based anode materials. (f) Nyquist plots before the cycle test and after 20 and 400 cycles. (g) Long cycling performance of FPTC hybrids and f-Ti_3C_2 at 5 A·g^{-1}.

attributed to the insertion of lithium ions into TiO_2 and the peaks at 1.04 and 0.71 V can be ascribed to the conversion reaction process of Fe_2O_3 nanoparticles to Li_2O and Fe^0 as well as the formation of solid electrolyte interface (SEI) [44, 45]. In subsequent cycles, the peak originally centered at 0.71 and 1.35 V positively shifts to 0.77 and 1.75 V, respectively, which might be due to polarization and formation of SEI film during electrochemical processes [47, 64]. A strong peak situated at around 2.0 V can be assigned to the oxidation process of Fe^0 to Fe^{3+} and extraction of Li^+ from Li_xTiO_2 in the anodic scan [57, 65]. More importantly, CV curves overlap with each other, manifesting superior reversibility and stable cycling stability.

The discharge and charge profiles of FPTC heterostructures at various current densities ranging from 50 mAh·g^{-1} to 8 A·g^{-1} are displayed in Fig. 4(b). It exhibits a discharge capacity of 795 mAh·g^{-1} and a charge capacity of 470 mAh·g^{-1} at 50 mA·g^{-1} in the first cycle. Thus, the initial coulombic efficiency equals to 59.11%, which is mainly due to the formation of SEI layer and other irreversible reactions between Li^+ and the functional groups terminated at MXene surface during the 1st cycle [18, 47, 66]. Figure 4(c) shows the cycling performance of f-Ti_3C_2 MXene and FPTC composites at 500 mA·g^{-1}. After 150 cycles, f-Ti_3C_2 MXene delivers a specific capacity of 142 mAh·g^{-1}, which is far lower than its theoretical capacity and can be ascribed to the surface termination groups (e.g., –OH, –F), thus impeding the insertion of Li ions into the interlayer (Fig. S5(a) in the ESM) [67]. It can be seen that the capacity of FPTC hybrids decreases within the very first cycles and then rises in the following cycles, which is identical to the discharge profiles at 1 A·g^{-1} (Fig. S5(b) in the ESM). The capacity fading might be assigned to the formation of unstable SEI layer and deterioration of electrode structure [18], while the capacity reactivation can be attributed to expanded interlayer spacing of f-Ti_3C_2 MXene and suppression of pulverization of Fe nanocomplex upon cycling [62]. What cannot be ignored is that *in-situ* formed TiO_2 plays multiple roles in electrochemical processes, which not only provides a smaller fraction of capacity owing to its low theoretical capacity but also enhances the structural stability of FPTC composites [52, 68, 69]. The main capacity contribution is from Fe_2O_3 owing to its high theoretical capacity [60, 70], together with more storage space caused by larger interlayer spacing of MXene, i.e., pillared structure [25, 27]. Finally, FPTC hybrids exhibits a high specific capacity of 535 mAh·g^{-1} after 150 cycles at 500 mA·g^{-1}, which exceeds previous reports [18, 52].

Figure 4(d) presents the rate performance of f-Ti_3C_2 MXene and FPTC heterostructures at different current densities from 50 mA·g^{-1} to 8 A·g^{-1}. For f-Ti_3C_2 MXene, a lower specific capacity of 392.8, 175.7, 144, 116.8, 95.6, 78.8, 58.1 and 57.2 mAh·g^{-1} can be attained at a current density of 0.05, 0.1, 0.2, 0.5, 1, 2, 5 and 8 A·g^{-1}, respectively. However, for FPTC hybrids, it shows an initial discharge capacity of 795 mAh·g^{-1} at 50 mA·g^{-1}. Upon increasing the current densities to 0.1, 0.2, 0.5, 1, 2, 5 and 8 A·g^{-1}, its specific capacity can be maintained at 434, 399, 371, 345, 320, 280 and 220 mAh·g^{-1}, respectively. Moreover, when the current density is turned back to 0.5 A·g^{-1}, a specific capacity of 450 mAh·g^{-1} after 20 cycles can still be recovered, signifying that FPTC hybrids deliver much better rate performance and reversibility when compared with various MXene-based materials at high current density (Fig. 4(e) and Table S3 in the ESM). The few-layered MXenes possess more active sites and are more accessible to electrolyte compared with multi-layered counterpart, thus facilitating electronic transfer, ionic diffusion. and showing one of the best rate capabilities [18, 33].

In order to further research the improved rate performance of FPTC composites, Fig. 4(f) compares the Nyquist plots of FPTC hybrids at initial state, 20th cycle and 400th cycle. It can be seen that all of them are composed of a depressed semicircle at high to medium frequency and an inclined line at low frequency. The diameter of depressed semicircle represents the faradic charge transfer resistance (R_{ct}) and the inclined line corresponds to the Warburg impedance that reflects the Li^+ diffusion into the electrode. In addition, the initial intercept at the real axis corresponds to the resistance of electrolyte (R_e) [71]. The simulated equivalent circuit and simulation results are shown in Fig. S6 and Table S2 in the ESM. As shown in Fig. S6 and Table S2 in the ESM, there is no SEI formation at initial state (before cycle). R_{SEI} gradually decreases as the cycles go on and reaches 2.02 Ω at 400th cycle, revealing the formation of stable SEI. FPTC electrode exhibits a relatively high R_{ct} of about 168 Ω at initial state. However, it shows a smaller semicircle as the cycles go on and R_{ct} reaches about 27.5 Ω at 400th cycle, which is due to the superior ionic and electronic conductivity of f-Ti_3C_2 MXene and activation process making the electrolyte easily penetrate into electrode [72, 73]. At the same time, the Li^+ ions diffusion kinetics in the FPTC electrode are closely connected to the slope line at the low frequency and the Li^+ ions diffusion coefficient (D) can be figured out by following equality [74]

$$D = 0.5R^2T^2/S^2n^4F^4C^2\sigma^2 \quad (2)$$

$$Z_{real} = R_s + R_{ct} + \sigma\omega^{-1/2} \quad (3)$$

R stands for ideal gas constant, T means the temperature, n denotes the number of electrons and σ represents the Warburg factor, which is identified by the slope of Z_{real} vs. $\omega^{-1/2}$ (Eq. (3)), and the D can be greatly enlarged with the decline of Warburg factor. It can be observed that the slope decreases sharply as the cycles go on (Fig. S7 in the ESM), manifesting an increase in D, which is mainly attributed to expanded interlayer spacing of MXene matrix. Likewise, a steeper slope for f-Ti_3C_2 MXene can be found compared with that of FPTC electrode (Fig. S8 in the ESM), indicating FPTC electrode ensures fast mobility of Li ions during the redox reaction processes.

The ultralong cycling performance of FPTC electrode and f-Ti_3C_2 MXene at 5 A·g^{-1} are illustrated in Fig. 4(g). It can be seen that FPTC electrodes deliver a high capacity of 310 mAh·g^{-1} after 850 cycles at 5 A·g^{-1}, which is higher than that of f-Ti_3C_2 (85 mAh·g^{-1}), indicating nanocomplex pillaring can indeed be an effective way to improve the capacity of f-Ti_3C_2 MXene. In the same way, the capacity of FPTC hybrids decreases at initial several cycles, then increases upon cycling and finally stabilizes. The improved lithium capacity and stabilization phenomenon can be mainly attributed to following reasons: (1) expanded interlayer distance of FPTC electrode which caused by volume expansion of Fe nanocomplex during lithiation processes can expose more potential storage space and permit more Li ions to be inserted into the interlayer [62]. (2) The presence of f-Ti_3C_2 MXene greatly improves the ionic, electronic and electrolyte accessibility and accommodate the volume expansion of Fe nanocomplexes upon cycling which in turn can impede the restacking of f-Ti_3C_2 MXene as a spacer [73]. (3) Ti-O-Fe chemical bonding can considerably maintain the electrode structure during Li^+ insertion/extraction processes [26]. (4) the *in-situ* formed TiO_2 can prevent the aggregation and pulverization of Fe nanocomplex owing to its electrochemical and mechanical stability [59].

To further explore the Li^+ ions storage mechanism, CV curves of FPTC heterostructures at initial state and after 2,000 cycles from 0.1 to 10 mV·s^{-1} are depicted in Fig. 5(a) and Fig. S9 in the ESM, respectively. The relationship between sweep rate(v)

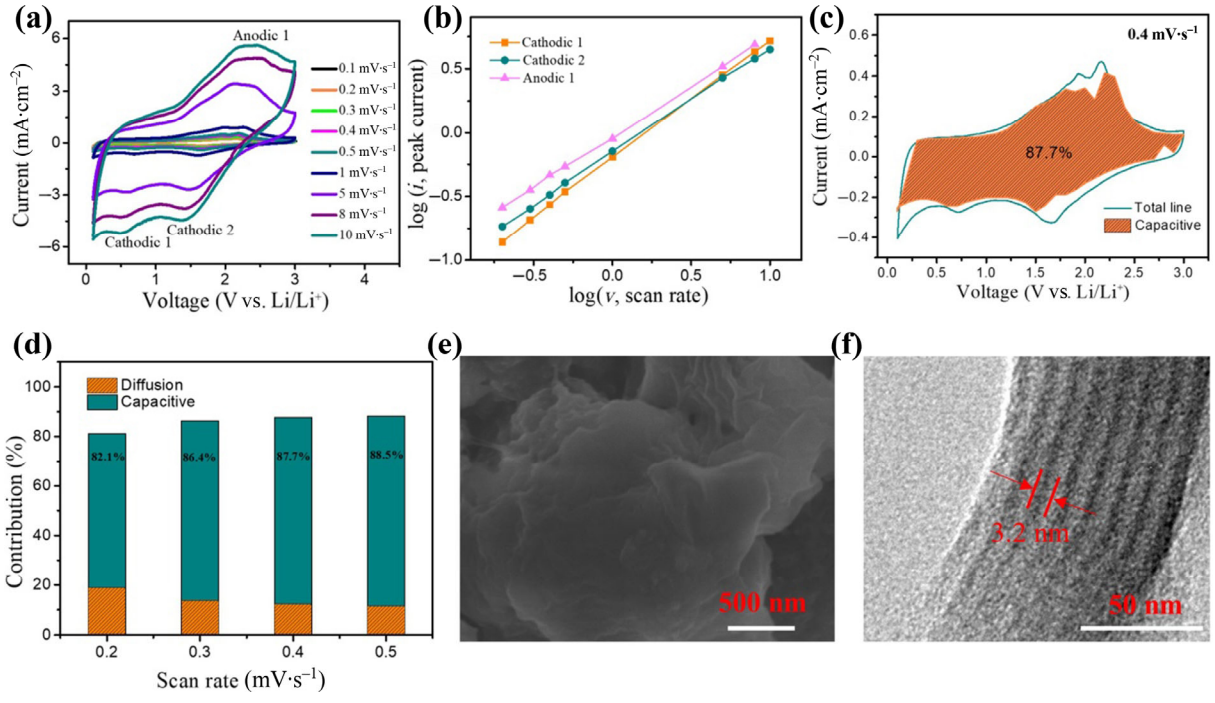

Figure 5 (a) CV curves of FPTC composites at various scan rates and (b) *b*-value determination of the peaks in CV curves. (c) CV curve with corresponding capacitive contribution at 0.4 mV·s^{-1}. (d) Capacitive contribution ratios at different sweep rate. (e) SEM image of the FPTC composites after 700 cycles. (f) HRTEM image of FPTC electrodes after 700 cycles.

and peak current (*i*) observes the following empirical power law [66]

$$i = av^b \quad (4)$$

both *a* and *b* are variable values. when *b* equals to 1, it indicates that a capacitive-controlled process governs the electrochemical reaction. $b = 0.5$ suggests a diffusion-controlled charge storage mechanism [75]. As illustrated in Fig. 5(b), the *b* values of cathodic 1, cathodic 2 and anodic peaks are 0.92, 0.82 and 0.79 (Fig. S10 in the ESM), respectively, manifesting the Li^+ ions storage mechanism of FPTC electrodes is dominated by capacitive behavior. The contribution of pseudocapacitive process can also be quantified by following equation [13]

$$i = k_1v + k_2v^{1/2} \quad (5)$$

where k_1v denotes capacitive contribution and $k_2v^{1/2}$ stands for diffusion contribution. It can be observed that the contribution of pseudocapacitive behavior to the total charge storage is close to 87.7% at 0.4 mV·s^{-1} (Fig. 5(c)). Furthermore, the percentage of pseudocapacitive contribution increases when the sweep rate increases from 0.2 to 0.5 mV·s^{-1} and reaches 88.5% at 0.5 mV·s^{-1} (Fig. 5(d)). The high proportion of pseudocapacitive contribution can be attributed to the ultrafine Fe nanocomplex which greatly shortens the ionic and electronic transport pathway [30]. More importantly, the f-Ti_3C_2 MXenes which possess 2D layered structure can exploit more surface active sites for the adsorption and desorption of Li^+ ions upon cycling, thus rendering high pseudocapacitive contribution [32, 76]. To sum up, the high pseudocapacitive contribution is conducive to the excellent charge transfer kinetics, thus leading to superior rate performance [74]. *Ex-situ* SEM and TEM images of FPTC hybrids after 700 cycles are also characterized to further explore changes in structure. As exhibited in Figs. 5(e) and 5(f). the structure of FPTC electrodes after 700 cycles charged to 3.0 V at 1 A·g^{-1} does not change significantly and the coarse surface transforms into smooth (Fig. S11 in the ESM), which might result in capacity reactivation [18]. It is also observed that the FPTC hybrids show an ultralarge interlayer spacing of 3.2 nm after 700 cycles discharged to 0 V (Fig. 5(f)), which might be caused by volume expansion of Fe nanocomplex upon continuous cycling [44], thus giving rise to capacity reactivation.

4 Conclusions

To sum up, fast preparation of f-Ti_3C_2 MXene which avoids serious restacking have been achieved based on the electrostatic attraction between negatively-charged f-Ti_3C_2 MXene and NH_4^+ ions. In order to improve electrochemical performance of f-Ti_3C_2 MXene and mediocre rate performance of cation-intercalated multi-layered MXene based anode materials, we have fabricated FPTC heterostructures by intercalating Fe ions into f-Ti_3C_2 MXene. FPTC electrode delivers a high capacity of 535 mAh·g^{-1} after 150 cycles at 0.5 A·g^{-1} and 310 mAh·g^{-1} after 850 cycles at 5 A·g^{-1} with no capacity loss, which can be ascribed to the stable electrode structure generated by Ti-O-Fe covalent bonding, superior Li^+ diffusion kinetics and electronic transfer from expanded interlayer distances of f-Ti_3C_2 MXene, the mechanical and electrochemical stability of *in-situ* formed TiO_2 and pillared few-layered structure. More importantly, f-Ti_3C_2 MXene can prevent the pulverization of Fe nanocomplex during lithiation/delithiation processes. The enhanced rate performance of FPTC heterostructures demonstrates the significance and feasibility of the pillared few-layered MXene structures. It is believed that the report will open a window for fabricating promising heterostructures with favorable rate capability which couples pillared few-layered MXenes with various metal compounds.

Acknowledgements

The authors are appreciative of the financial support by the Tai hu Electric Corporation 0001 and the National Natural Science Foundation of China (No. 51901206).

Electronic Supplementary Material: Supplementary material

(XPS spectrum of few-layered Ti_3C_2 MXene, SEM images of Ti_3AlC_2 MAX, multi-layered Ti_3C_2 MXene and few-layered Ti_3C_2 MXene, EIS spectra of few-layered Ti_3C_2 MXene and FPTC hybrids, simulated equivalent circuit, electrochemical performance of few-layered Ti_3C_2 MXene and FPTC hybrids, summary of electrochemical performance of different MXene-based composites at low current density and high current density) is available in the online version of this article at https://doi.org/10.1007/s12274-020-3221-y.

References

[1] Li, X. L.; Zhi, L. J. Graphene hybridization for energy storage applications. *Chem. Soc. Rev.* **2018**, *47*, 3189–3216.

[2] Tu, F. Z.; Han, Y.; Du, Y. C.; Ge, X. F.; Weng, W. S.; Zhou, X. S.; Bao, J. C. Hierarchical nanospheres constructed by ultrathin MoS_2 nanosheets braced on nitrogen-doped carbon polyhedra for efficient lithium and sodium storage. *ACS Appl. Mater. Interfaces* **2019**, *11*, 2112–2119.

[3] Tan, C. L.; Cao, X. H.; Wu, X. J.; He, Q. Y.; Yang, J.; Zhang, X.; Chen, J. Z.; Zhao, W.; Han, S. K.; Nam, G. H. et al. Recent advances in ultrathin two-dimensional nanomaterials. *Chem. Rev.* **2017**, *117*, 6225–6331.

[4] Naguib, M.; Kurtoglu, M.; Presser, V.; Lu, J.; Niu, J. J.; Heon, M.; Hultman, L.; Gogotsi, Y.; Barsoum, M. W. Two-dimensional nanocrystals produced by exfoliation of Ti_3AlC_2. *Adv. Mater.* **2011**, *23*, 4248–4253.

[5] Song, X. L.; Wang, H.; Jin, S. M.; Lv, M.; Zhang, Y.; Kong, X. D.; Xu, H. M.; Ma, T.; Luo, X. Y.; Tan, H. F. et al. Oligolayered $Ti_3C_2T_x$ MXene towards high performance lithium/sodium storage. *Nano Res.* **2020**, *13*, 1659–1667.

[6] Nan, J. X.; Guo, X.; Xiao, J.; Li, X.; Chen, W. H.; Wu, W. J.; Liu, H.; Wang, Y.; Wu, M. H.; Wang, G. X. Nanoengineering of 2D MXene-based materials for energy storage applications. *Small* **2019**, 1902085.

[7] Guo, X.; Xie, X. Q.; Choi, S.; Zhao, Y. F.; Liu, H.; Wang, C. Y.; Chang, S.; Wang, G. X. Sb_2O_3/MXene($Ti_3C_2T_x$) hybrid anode materials with enhanced performance for sodium-ion batteries. *J. Mater. Chem. A* **2017**, *5*, 12445–12452.

[8] Guo, X.; Zhang, W. X.; Zhang, J. Q.; Zhou, D.; Tang, X.; Xu, X. F.; Li, B. H.; Liu, H.; Wang, G. X. Boosting sodium storage in two-dimensional phosphorene/$Ti_3C_2T_x$ MXene nanoarchitectures with stable fluorinated interphase. *ACS Nano* **2020**, *14*, 3651–3659.

[9] Dong, Y. F.; Wu, Z. S.; Zheng, S. H.; Wang, X. H.; Qin, J. Q.; Wang, S.; Shi, X. Y.; Bao, X. H. Ti_3C_2 MXene-derived sodium/potassium titanate nanoribbons for high-performance sodium/potassium ion batteries with enhanced capacities. *ACS Nano* **2017**, *11*, 4792–4800.

[10] Narayanasamy, M.; Kirubasankar, B.; Shi, M. J.; Velayutham, S.; Wang, B.; Angaiah, S.; Yan, C. Morphology restrained growth of V_2O_5 by the oxidation of V-MXenes as a fast diffusion controlled cathode material for aqueous zinc ion batteries. *Chem. Commun.* **2020**, *56*, 6412–6415.

[11] Li, Z. Y.; Wang, X. X.; Zhang, W. M.; Yang, S. P. Two-dimensional Ti_3C_2@CTAB-Se (MXene) composite cathode material for high-performance rechargeable aluminum batteries. *Chem. Eng. J.* **2020**, *398*, 125679.

[12] Tang, Q.; Zhou, Z.; Shen, P. W. Are MXenes promising anode materials for Li ion batteries? Computational studies on electronic properties and Li storage capability of Ti_3C_2 and $Ti_3C_2X_2$ (X = F, OH) monolayer. *J. Am. Chem. Soc.* **2012**, *134*, 16909–16916.

[13] Hui, X. B.; Zhao, R. Z.; Zhang, P.; Li, C. X.; Wang, C. X.; Yin, L. W. Low-temperature reduction strategy synthesized Si/Ti_3C_2 MXene composite anodes for high-performance Li-ion batteries. *Adv. Energy Mater.* **2019**, *9*, 1901065.

[14] Ying, H. J.; Zhang, S. L.; Meng, Z.; Sun, Z. X.; Han, W. Q. Ultrasmall Sn nanodots embedded inside N-doped carbon microcages as high-performance lithium and sodium ion battery anodes. *J. Mater. Chem. A* **2017**, *5*, 8334–8342.

[15] Zhang, Q. B.; Chen, H. X.; Luo, L. L.; Zhao, B. T.; Luo, H.; Han, X.; Wang, J. W.; Wang, C. M.; Yang, Y.; Zhu, T. et al. Harnessing the concurrent reaction dynamics in active Si and Ge to achieve high performance lithium-ion batteries. *Energy Environ. Sci.* **2018**, *11*, 669–681.

[16] Sun, D. D.; Wang, M. S.; Li, Z. Y.; Fan, G. X.; Fan, L. Z.; Zhou, A. G. Two-dimensional Ti_3C_2 as anode material for Li-ion batteries. *Electrochem. Commun.* **2014**, *47*, 80–83.

[17] Xie, Y.; Naguib, M.; Mochalin, V. N.; Barsoum, M. W.; Gogotsi, Y.; Yu, X. Q.; Nam, K. W.; Yang, X. Q.; Kolesnikov, A. I.; Kent, P. R. C. Role of surface structure on Li-ion energy storage capacity of two-dimensional transition-metal carbides. *J. Am. Chem. Soc.* **2014**, *136*, 6385–6394.

[18] Wang, Y. S.; Li, Y. Y.; Qiu, Z. P.; Wu, X. Z.; Zhou, P. F.; Zhou, T.; Zhao, J. P.; Miao, Z. C.; Zhou, J.; Zhuo, S. P. Fe_3O_4@Ti_3C_2 MXene hybrids with ultrahigh volumetric capacity as an anode material for lithium-ion batteries. *J. Mater. Chem. A* **2018**, *6*, 11189–11197.

[19] Ai, J. J.; Lei, Y. K.; Yang, S.; Lai, C. Y.; Xu, Q. J. SnS nanoparticles anchored on Ti_3C_2 nanosheets matrix via electrostatic attraction method as novel anode for lithium ion batteries. *Chem. Eng. J.* **2019**, *357*, 150–158.

[20] Ali, A.; Hantanasirisakul, K.; Abdala, A.; Urbankowski, P.; Zhao, M. Q.; Anasori, B.; Gogotsi, Y.; Aïssa, B.; Mahmoud, K. A. Effect of synthesis on performance of MXene/Iron oxide anode material for lithium-ion batteries. *Langmuir* **2018**, *34*, 11325–11334.

[21] Jun, B. M.; Kim, S.; Heo, J.; Park, C. M.; Her, N.; Jang, M.; Huang, Y.; Han, J.; Yoon, Y. Review of MXenes as new nanomaterials for energy storage/delivery and selected environmental applications. *Nano Res.* **2019**, *12*, 471–487.

[22] Xie, X. Q.; Zhao, M. Q.; Anasori, B.; Maleski, K.; Ren, C. E.; Li, J. W.; Byles, B. W.; Pomerantseva, E.; Wang, G. X.; Gogotsi, Y. Porous heterostructured MXene/carbon nanotube composite paper with high volumetric capacity for sodium-based energy storage devices. *Nano Energy* **2016**, *26*, 513–523.

[23] Guo, X.; Zhang, J. Q.; Song, J. J.; Wu, W. J.; Liu, H.; Wang, G. X. MXene encapsulated titanium oxide nanospheres for ultra-stable and fast sodium storage. *Energy Storage Mater.* **2018**, *14*, 306–313.

[24] Zhang, S. L.; Ying, H. J.; Guo, R. N.; Yang, W. T.; Han, W. Q. Vapor deposition red phosphorus to prepare nitrogen-doped $Ti_3C_2T_x$ MXenes composites for lithium-ion batteries. *J. Phys. Chem. Lett.* **2019**, *10*, 6446–6454.

[25] Wang, C. D.; Xie, H.; Chen, S. M.; Ge, B. H.; Liu, D. B.; Wu, C. Q.; Xu, W. J.; Chu, W. S.; Babu, G.; Ajayan, P. M. et al. Atomic cobalt covalently engineered interlayers for superior lithium-ion storage. *Adv. Mater.* **2018**, *30*, 1802525.

[26] Wang, C. D.; Chen, S. M.; Xie, H.; Wei, S. Q.; Wu, C. Q.; Song, L. Atomic Sn^{4+} decorated into vanadium carbide MXene interlayers for superior lithium storage. *Adv. Energy Mater.* **2019**, *9*, 1802977.

[27] Luo, J. M.; Zhang, W. K.; Yuan, H. D.; Jin, C. B.; Zhang, L. Y.; Huang, H.; Liang, C.; Xia, Y.; Zhang, J.; Gan, Y. P. et al. Pillared structure design of MXene with ultralarge interlayer spacing for high-performance lithium-ion capacitors. *ACS Nano* **2017**, *11*, 2459–2469.

[28] Yang, L. S.; Chen, W. J.; Yu, Q. M.; Liu, B. L. Mass production of two-dimensional materials beyond graphene and their applications. *Nano Res.*, in press, DOI: 10.1007/s12274-020-2897-3.

[29] Zeng, X. Q.; Li, M.; El-Hady, D. A.; Alshitari, W.; Al-Bogami, A. S.; Lu, J.; Amine, K. Commercialization of lithium battery technologies for electric vehicles. *Adv. Energy Mater.* **2019**, *9*, 1900161.

[30] Hu, Z.; Liu, Q. N.; Chou, S. L.; Dou, S. X. Advances and challenges in metal sulfides/selenides for next-generation rechargeable sodium-ion batteries. *Adv. Mater.* **2017**, *29*, 1700606.

[31] Luo, S. J.; Xie, L. Y.; Han, F.; Wei, W.; Huang, Y.; Zhang, H.; Zhu, M. S.; Schmidt, O. G.; Wang, L. Nanoscale parallel circuitry based on interpenetrating conductive assembly for flexible and high-power zinc ion battery. *Adv. Funct. Mater.* **2019**, *29*, 1901336.

[32] Chao, D. L.; Zhu, C. R.; Yang, P. H.; Xia, X. H.; Liu, J. L.; Wang, J.; Fan, X. F.; Savilov, S. V.; Lin, J. Y.; Fan, H. J. et al. Array of nanosheets render ultrafast and high-capacity Na-ion storage by tunable pseudocapacitance. *Nat. Commun.* **2016**, *7*, 12122.

[33] Wu, Y. T.; Nie, P.; Wang, J.; Dou, H.; Zhang, X. G. Few-layer MXenes delaminated via high-energy mechanical milling for enhanced

sodium-ion batteries performance. *ACS Appl. Mater. Interfaces*. **2017**, *9*, 39610–39617.

[34] Zhang, L. Y.; Chen, L.; Luo, H.; Zhou, X. F.; Liu, Z. P. Large-sized few-layer graphene enables an ultrafast and long-life aluminum-ion battery. *Adv. Energy Mater*. **2017**, *7*, 1700034.

[35] Zhang, S. L.; Han, W. Q. Recent advances in MXenes and their composites in lithium/sodium batteries from the viewpoints of components and interlayer engineering. *Phys. Chem. Chem. Phys*. **2020**, *22*, 16482–16526.

[36] Naguib, M.; Mashtalir, O.; Carle, J.; Presser, V.; Lu, J.; Hultman, L.; Gogotsi Y.; Barsoum M. W. Two-dimensional transition metal carbides. *ACS Nano* **2012**, *6*, 1322–1331.

[37] Luo, J. M.; Wang, C. L.; Wang, H.; Hu, X. F.; Matios, E.; Lu, X.; Zhang, W. K.; Tao, X. Y.; Li, W. Y. Pillared MXene with ultralarge interlayer spacing as a stable matrix for high performance sodium metal anodes. *Adv. Funct. Mater*. **2019**, *29*, 1805946.

[38] Luo, J. M.; Tao, X. Y.; Zhang, J.; Xia, Y.; Huang, H.; Zhang, L. Y.; Gan, Y. P.; Liang, C.; Zhang, W. K. Sn^{4+} ion decorated highly conductive Ti_3C_2 MXene: Promising lithium-ion anodes with enhanced volumetric capacity and cyclic performance. *ACS Nano* **2016**, *10*, 2491–2499.

[39] Luo, J. M.; Zheng, J. H.; Nai, J. W.; Jin, C. B.; Yuan, H. D.; Sheng, O. W.; Liu, Y. J.; Fang, R. Y.; Zhang, W. K.; Huang, H. et al. Atomic sulfur covalently engineered interlayers of Ti_3C_2 MXene for ultra-fast sodium-ion storage by enhanced pseudocapacitance. *Adv. Funct. Mater*. **2019**, *29*, 1808107.

[40] Xu, M.; Lei, S. L.; Qi, J.; Dou, Q. Y.; Liu, L. Y.; Lu, Y. L.; Huang, Q.; Shi, S. Q.; Yan, X. B. Opening magnesium storage capability of two-dimensional mxene by intercalation of cationic surfactant. *ACS Nano* **2018**, *12*, 3733–3740.

[41] Li, Y. Y.; Huang, Y.; Ou, C. Z.; Zhu, J. L.; Yuan, X. X.; Yan, L.; Li, W. W.; Zhang, H. Y. Enhanced capability and cyclability of flexible TiO_2-reduced graphene oxide hybrid paper electrode by incorporating monodisperse anatase TiO_2 quantum dots. *Electrochim. Acta*. **2018**, *259*, 474–484.

[42] Anasori, B.; Lukatskaya, M. R.; Gogotsi, Y. 2D metal carbides and nitrides (MXenes) for energy storage. *Nat. Rev. Mater*. **2017**, *2*, 16098.

[43] Zhang, C. J.; Pinilla, S.; McEvoy, N.; Cullen, C. P.; Anasori, B.; Long, E.; Park, S. H.; Seral-Ascaso, A.; Shmeliov, A.; Krishnan, D. et al. Oxidation stability of colloidal two-dimensional titanium carbides (MXenes). *Chem. Mater*. **2017**, *29*, 4848–4856.

[44] Yang, J. L.; Wu, Q. L.; Yang, X. F.; He, S. M.; Khan, J.; Meng, Y. Y.; Zhu, X. M.; Tong, S. F.; Wu, M. M. Chestnut-like TiO_2@α-Fe_2O_3 core–shell nanostructures with abundant interfaces for efficient and ultralong life lithium-ion storage. *ACS Appl. Mater. Interfaces* **2016**, *9*, 354–361.

[45] Chen, Y. B.; Liang, J. H.; Tian, Q. H.; Zhang, W.; Sui, Z. Y. Facile construction of clustered Fe_2O_3/TiO_2 composite for improved lithium storage performance. *Synth. Met*. **2020**, *263*, 116353.

[46] Lian, P. C.; Dong, Y. F.; Wu, Z. S.; Zheng, S. H.; Wang, X. H.; Wang, S.; Sun, C. L.; Qin, J. Q.; Shi, X. Y.; Bao, X. H. Alkalized Ti_3C_2 MXene nanoribbons with expanded interlayer spacing for high-capacity sodium and potassium ion batteries. *Nano Energy* **2017**, *40*, 1–8.

[47] Zhao, D. Y.; Zhao, R. Z.; Dong, S. H.; Miao, X. G.; Zhang, Z. W.; Wang, C. X.; Yin, L. W. Alkali-induced 3D crinkled porous Ti_3C_2 MXene architectures coupled with NiCoP bimetallic phosphide nanoparticles as anodes for high-performance sodium-ion batteries. *Energy Environ. Sci*. **2019**, *12*, 2422–2432.

[48] Zhao, D.; Clites, M.; Ying, G. B.; Kota, S.; Wang, J.; Natu, V.; Wang, X.; Pomerantseva, E.; Cao, M. H.; Barsoum, M. W. Alkali-induced crumpling of $Ti_3C_2T_x$ (MXene) to form 3D porous networks for sodium ion storage. *Chem. Commun*. **2018**, *54*, 4533–4536.

[49] Peng, L. L.; Fang, Z. W.; Zhu, Y.; Yan, C. S.; Yu, G. H. Holey 2D nanomaterials for electrochemical energy storage. *Adv. Energy Mater*. **2018**, *8*, 1702179.

[50] Liu, H.; Zhang, X.; Zhu, Y. F.; Cao, B.; Zhu, Q. Z.; Zhang, P.; Xu, B.; Wu, F.; Chen, R. J. Electrostatic self-assembly of 0D–2D SnO_2 quantum dots/$Ti_3C_2T_x$ MXene hybrids as anode for lithium-ion batteries. *Nano-Micro Lett*. **2019**, *11*, 65.

[51] Ni, Q.; Dong, R. Q.; Bai, Y.; Wang, Z. H.; Ren, H. X.; Sean, S.; Wu, F.; Xu, H. J.; Wu, C. Superior sodium-storage behavior of flexible anatase TiO_2 promoted by oxygen vacancies. *Energy Storage Mater*. **2020**, *25*, 903–911.

[52] Liu, Y. T.; Zhang, P.; Sun, N.; Anasori, B.; Zhu, Q. Z.; Liu, H.; Gogotsi, Y.; Xu, B. Self-assembly of transition metal oxide nanostructures on MXene nanosheets for fast and stable lithium storage. *Adv. Mater*. **2018**, *30*, 1707334.

[53] Hung, W. C.; Chen, Y. C.; Chu, H.; Tseng, T. K. Synthesis and characterization of TiO_2 and Fe/TiO_2 nanoparticles and their performance for photocatalytic degradation of 1, 2-dichloroethane. *Appl. Surf. Sci*. **2008**, *255*, 2205–2213.

[54] Chen, X. B.; Liu, L.; Yu, P. Y.; Mao, S. S. Increasing solar absorption for photocatalysis with black hydrogenated titanium dioxide nanocrystals. *Science* **2011**, *331*, 746.

[55] Yamashita, T.; Hayes, P. Analysis of XPS spectra of Fe^{2+} and Fe^{3+} ions in oxide materials. *Appl. Surf. Sci*. **2008**, *254*, 2441–2449.

[56] Tong, T. Z.; Zhang, J. L.; Tian, B. Z.; Chen, F.; He, D. N. Preparation of Fe^{3+}-doped TiO_2 catalysts by controlled hydrolysis of titanium alkoxide and study on their photocatalytic activity for methyl orange degradation. *J. Hazard. Mater*. **2008**, *155*, 572–579.

[57] Zhang, Z. Y.; Weng, L.; Rao, Q. S.; Yang, S. D.; Hu, J. Q.; Cai, J. J.; Min, Y. G. Highly-dispersed iron oxide nanoparticles anchored on crumpled nitrogen-doped MXene nanosheets as anode for Li-ion batteries with enhanced cyclic and rate performance. *J. Power Sources* **2019**, *439*, 227107.

[58] Zheng, W.; Zhang, P.; Chen, J.; Tian, W. B.; Zhang, Y. M.; Sun, Z. M. *In situ* synthesis of CNTs@Ti_3C_2 hybrid structures by microwave irradiation for high-performance anodes in lithium ion batteries. *J. Mater. Chem. A* **2018**, *6*, 3543–3551.

[59] Hou, S.; Wang, P.; Li, Y. P.; Pang, F.; Liu, M.; Luo, Y. Z.; Zhuang, L.; Zhao, L. Z. Podocarpus-like α-Fe_2O_3/TiO_2 composite with balsam pear texture for enhanced lithium storage. *Appl. Surf. Sci*. **2019**, *476*, 959–965.

[60] Yin, L. H.; Gao, Y. J.; Jeon, I.; Yang, H.; Kim, J. P.; Jeong, S. Y.; Cho, C. R. Rice-panicle-like γ-Fe_2O_3@C nanofibers as high-rate anodes for superior lithium-ion batteries. *Chem. Eng. J*. **2019**, *356*, 60–68.

[61] Zou, G. D.; Zhang, Z. W.; Guo, J. X.; Liu, B. Z.; Zhang, Q. R.; Fernandez, C.; Peng, Q. M. Synthesis of MXene/Ag composites for extraordinary long cycle lifetime lithium storage at high rates. *ACS Appl. Mater. Interfaces* **2016**, *8*, 22280–22286.

[62] Fang, R. Y.; Lu, C. W.; Chen, A. Q.; Wang, K.; Huang, H.; Gan, Y. P.; Liang, C.; Zhang, J.; Tao, X. Y.; Xia, Y. et al. 2D MXene-based energy storage materials: Interfacial structure design and functionalization. *ChemSusChem* **2019**, *13*, 1409–1419.

[63] Deng, Y. Q.; Shang, T. X.; Wu, Z. T.; Tao, Y.; Luo, C.; Liang, J. C.; Han, D. L.; Lyu, R. Y.; Qi, C. S.; Lv, W. et al. Fast gelation of $Ti_3C_2T_x$ MXene initiated by metal ions. *Adv. Mater*. **2019**, *31*, 1902432.

[64] Zhu, K.; Zhang, Y.; Qiu, H. L.; Meng, Y.; Gao, Y.; Meng, X.; Gao, Z. M.; Chen, G.; Wei, Y. J. Hierarchical Fe_3O_4 microsphere/reduced graphene oxide composites as a capable anode for lithium-ion batteries with remarkable cycling performance. *J. Alloys Compd*. **2016**, *675*, 399–406.

[65] Li, Y.; Wang, S.; Lei, D. N.; He, Y. B.; Li, B. H.; Kang, F. Y. Acetic acid-induced preparation of anatase TiO_2 mesocrystals at low temperature for enhanced Li-ion storage. *J. Mater. Chem. A* **2017**, *5*, 12236–12242.

[66] Zhang, P.; Wang, D. J.; Zhu, Q. Z.; Sun, N.; Fu, F.; Xu, B. Plate-to-layer Bi_2MoO_6/MXene-Heterostructured anode for lithium-ion batteries. *Nano-Micro Lett*. **2019**, *11*, 81.

[67] Hemanth, N. R.; Kandasubramanian, B. Recent advances in 2D MXenes for enhanced cation intercalation in energy harvesting applications: A review. *Chem. Eng. J*. **2020**, *392*, 123678.

[68] Gao, L.; Hu, H.; Li, G. J.; Zhu, Q. C.; Yu, Y. Hierarchical 3D TiO_2@Fe_2O_3 nanoframework arrays as high-performance anode materials. *Nanoscale* **2014**, *6*, 6463–6467.

[69] Yang, C.; Liu, Y.; Sun, X.; Zhang, Y. R.; Hou, L. R.; Zhang, Q. A.; Yuan, C. Z. *In-situ* construction of hierarchical accordion-like

TiO_2/Ti_3C_2 nanohybrid as anode material for lithium and sodium ion batteries. *Electrochim. Acta* **2018**, *271*, 165–172.

[70] Zhang, S. L.; Guan, B. Y.; Wu, H. B.; Lou, X. W. D. Metal-organic framework-assisted synthesis of compact Fe_2O_3 nanotubes in Co_3O_4 host with enhanced lithium storage properties. *Nano-Micro Lett.* **2018**, *10*, 44.

[71] Guo, R. N.; Zhang, S. L.; Ying, H. J.; Yang, W. T.; Wang, J. L.; Han, W. Q. New, effective, and low-cost dual-functional binder for porous silicon anodes in lithium-ion batteries. *ACS Appl. Mater. Interfaces*. **2019**, *11*, 14051–14058.

[72] Zhang, Y.; Niu, Y. B.; Wang, M. Q.; Yang, J. G.; Lu, S. Y.; Han, J.; Bao, S. J.; Xu, M. W. Exploration of a calcium-organic framework as an anode material for sodium-ion batteries. *Chem. Commun.* **2016**, *52*, 9969–9971.

[73] Xiong, D. B.; Li, X. F.; Bai, Z. M.; Lu, S. G. Recent advances in layered $Ti_3C_2T_x$ MXene for electrochemical energy storage. *Small* **2018**, *14*, 1703419.

[74] Zhong, W.; Tao, M. L.; Tang, W. W.; Gao, W.; Yang, T. T.; Zhang, Y. Q.; Zhan, R. M.; Bao, S. J.; Xu, M. W. MXene-derivative pompon-like $Na_2Ti_3O_7$@C anode material for advanced sodium ion batteries. *Chem. Eng. J.* **2019**, *378*, 122209.

[75] Hu, Z. L.; Kuai, X. X.; Chen, J. T.; Sun, P. F.; Zhang, Q. B.; Wu, H. H.; Zhang, L. Strongly coupled MoS_2 nanocrystal/Ti_3C_2 nanosheet hybrids enable high-capacity lithium-ion storage. *ChemSusChem* **2020**, *13*, 1485–1490.

[76] Huang, H. W.; Cui, J.; Liu, G. X.; Bi, R.; Zhang, L. Carbon-coated $MoSe_2$/MXene hybrid nanosheets for superior potassium storage. *ACS Nano* **2019**, *13*, 3448–3456.